

Confinement transitions driven by ion heating in reduced model turbulence simulations

D. A. Russell and J. R. Myra

Lodestar Research Corporation, Boulder, CO, USA

March 2017

DOE-ER/54392-85

LRC-17-169

LODESTAR RESEARCH CORPORATION

*2400 Central Avenue
Boulder, Colorado 80301*

Confinement transitions driven by ion heating in reduced model turbulence simulations

D. A. Russell and J. R. Myra

Lodestar Research Corporation, 2400 Central Avenue, Boulder, Colorado 80301

Abstract

A two-dimensional, electrostatic reduced turbulence model with parallel physics closure relations and ion pressure dynamics has been applied to study confinement transitions driven by ion heating. Low (L) and high (H) confinement regimes are observed in these SOLT code simulations, depending on the strength of an ion heating source localized inside the separatrix: with increasing heating, particle and energy confinement times at first decrease in the L-mode then rise in the H-mode. The L-H transition is marked by distinct changes in sheared-flow profiles. The addition of ion pressure dynamics enables modeling the self-consistent interaction between the ion diamagnetic drift and the radial electric field (mean and zonal flows). The roles of these sheared flows in mediating the L-H transition are explored for both ramped heating and steady state cases. Finally it is shown that the scrape-off layer collisionality regime, specifically sheath connected or conduction limited, has a profound effect on confinement in the closed surface region.

Keywords: plasma turbulence, simulation, confinement transitions, sheared flow, scrape-off layer

I. Introduction

Magnetically confined tokamak plasmas have long been known to transition under certain conditions to a self-organized state which exhibits enhanced confinement.¹ This transition to the high confinement (H-mode) state is important for good plasma energy confinement in present day devices, and critical for ITER to allow achievement of its burning plasma goals. Shearing by radially varying ExB drifts is thought to play a central mechanistic role in suppressing turbulent transport and enabling the low confinement to high confinement (L-H) transition but despite many years of investigation, a complete and generally accepted theory of the transition is not presently available. Transition dynamics in theory and experiment have been discussed in a number of recent papers.²⁻⁸ The L-H transition has also been simulated by a variety of numerical models.⁹⁻¹⁵ These papers have emphasized different physical effects including the importance of neoclassical flows, turbulent Reynolds stress, ion pressure gradients and ion orbit loss. A recent review of the role of turbulence-flow interactions covering experiment, theory and simulation has been given by Schmitz¹⁶.

In the present work, we apply the SOLT code¹⁷ to the L-H transition problem. A recent version of the SOLT model,¹⁸ summarized in Sec. II, is employed for these studies. The model retains ion pressure dynamics and a generalized vorticity (which does not employ the Boussinesq approximation). Our work complements previously published work in several respects. We highlight the role of ramped heating effects and a moving front in triggering a confinement transition in Sec. III. Transient effects have been studied theoretically¹⁹ and moving fronts have been observed in some experiments.^{4,5,20,21} Steady state simulations in Sec. III are also shown to result in different confinement regimes in our model. In Sec. IV, for the first time, to best of our knowledge, the role of scrape-off layer conditions on edge/core confinement conditions is explored. This topic is of particular relevance to future fusion devices because it is anticipated that reactor-relevant regimes may require a collisional dissipative SOL to mitigate the intense heat flux exhaust channel, which would likely imply operation in a semi-detached regime. The compatibility of such a regime with good core H-mode confinement is a topic of some concern. A summary and conclusions is given in Sec. IV. Finally in an Appendix we generalize the usual cold fluid Boussinesq description of turbulent energetics to the finite ion pressure non-Boussinesq model.

II. The SOLT code model

The scrape-off layer turbulence (SOLT) code is a 2D electrostatic fluid turbulence code which describes plasma dynamics in the two-dimensional (x,y) Cartesian plane perpendicular to

the magnetic field for flute-like modes. Here x and y are the radial and binormal (approximately poloidal) coordinates. The model, described in detail in Ref. 18 consists of coupled equations in x , y and time t for the quasi-neutral density n , electron and ion temperatures T_e and T_i , and generalized vorticity, $\rho = -\nabla \cdot (n\nabla\Phi + \nabla p_i)$ where Φ is the electrostatic potential, and $p_i = nT_i$ is the ion pressure. The electrostatic potential is extracted from the vorticity by different algorithms depending on the problem: relaxation,²² conjugate gradient and multigrid. Note that the Boussinesq approximation is not invoked.

All fields in SOLT are turbulent, i.e. $n = n(x,y,t)$, etc. and no scale separation is employed in the evolution equations: fluctuations are evolved together with the background (y -averaged fields) without expanding about ambient profiles. Self-consistent order unity fluctuations are supported. In the parallel direction, the dynamics are treated by analytical closure relations. In the closed surface region, the model is a superset of the Wakatani-Hasegawa model,²³ to allow a rudimentary description of drift-wave physics. In the scrape-off layer (SOL) the model dynamically transitions between sheath-connected and conduction limited regimes depending on the local collisionality. SOLT contains a reduced description of the electron drift wave, interchange and Kelvin-Helmholtz (K-H) instabilities, as well as sheath physics and blob propagation. Important for the present study, which models H-mode regimes, is the self-consistent evolution of ion pressure and ion diamagnetic drifts, where the latter is allowed to be comparable to the $E \times B$ drift.

In the simulations presented in this report, particle and energy fluxes are driven by diffused (D) Gaussian sources (S) localized in a buffer zone near the core-side boundary. This injection region is well removed from the separatrix ($\Delta x = 0$) in the simulations and thus effectively implements flux-driven boundary conditions for the simulation region of most interest. The SOL ($x > 0$) is defined in practice by the region where parallel sheath or conduction end-losses are invoked.

We will find in Secs. III and IV that the confinement of the core-edge region ($x < 0$) is controlled primarily by the strength of the ion heating source, and, in Sec. V by the parameter regime of the SOL. The primary diagnostics that we employ for the L-H transition, are the steepness of the pressure gradient and the particle and energy confinement times defined by

$$\tau_n = \frac{\int_{x<0} dx \langle n \rangle}{\int_{x<0} dx S_n}, \quad (1)$$

$$\tau_p = \frac{\int_{x<0} dx \langle p \rangle}{\int_{x<0} dx S_p}. \quad (2)$$

III. L-H transition for an “ramped” ion heating source

In most of this section, we present results from a single SOLT simulation driven by a diffused ion heating source, confined near the core-side boundary, that grows linearly with time: a “ramped” source, illustrated in Fig. 1. The parameters of the simulation are typical of NSTX. We simulate a deuterium plasma with reference density $n_0 = 10^{13} \text{ cm}^{-3}$ and reference temperature $T_0 = 100 \text{ eV}$, in an outboard midplane magnetic field of $B = 3416 \text{ Gauss}$. At these reference parameters, the ion Larmor radius is $\rho_s = 4.2 \text{ mm}$, the ion cyclotron frequency is $\Omega_i/2\pi = 2.6 \text{ MHz}$, and the ion sound speed is $c_s = 69 \text{ km/sec}$. To convert the dimensionless Bohm units used in the SOLT code to physical units of length, time, velocity, energy and electrostatic potential we use ρ_s , $(\Omega_i/2\pi)^{-1} = 0.4 \mu\text{s}$, c_s , T_0 and T_0/e , respectively, where e is the magnitude of the electron’s charge ($1.6022 \cdot 10^{-19} \text{ Coulomb}$). In Bohm units, the growth rate of the interchange instability, squared, is $\gamma_{\text{mhd}}^2 = -(2\rho_s/R) \partial_x(P_e+P_i)/n$, where the major radius of the tokamak (NSTX) is $R = 144 \text{ cm}$.

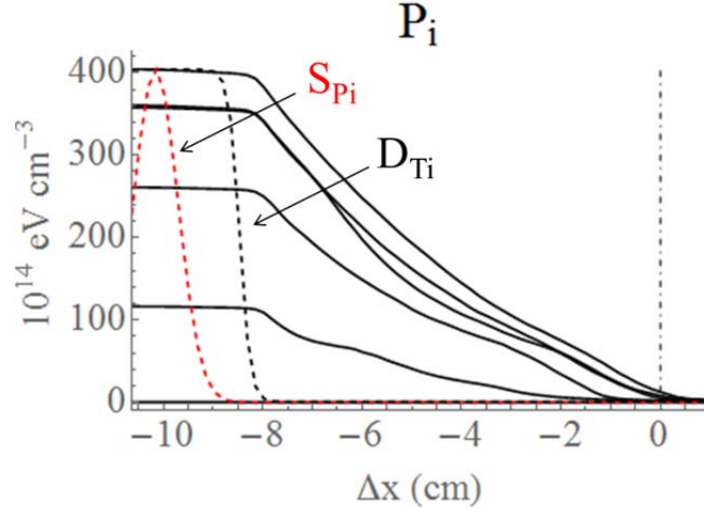


Fig. 1. Illustration of the ion heating source (S_{P_i}) and diffusion profiles (D_{T_i}) used to create a flux-driven boundary condition, together with the growing ion pressure sampled at 0, 0.5, 1.0, 1.5, 2.0 and 2.5 ms, starting from a flat P_i profile at $t = 0$, for the ramped-source case. The dot-dashed line at $\Delta x = 0$ denotes the separatrix.

As the simulation progresses, three confinement regimes are visited successively: low (L), high (H) and avalanche (A). The transitions between regimes correspond to the propagation of an ion pressure front, viz. high-gradient domain, from the core region to the edge. The front is shown passing a reference point in Fig. 2(a).

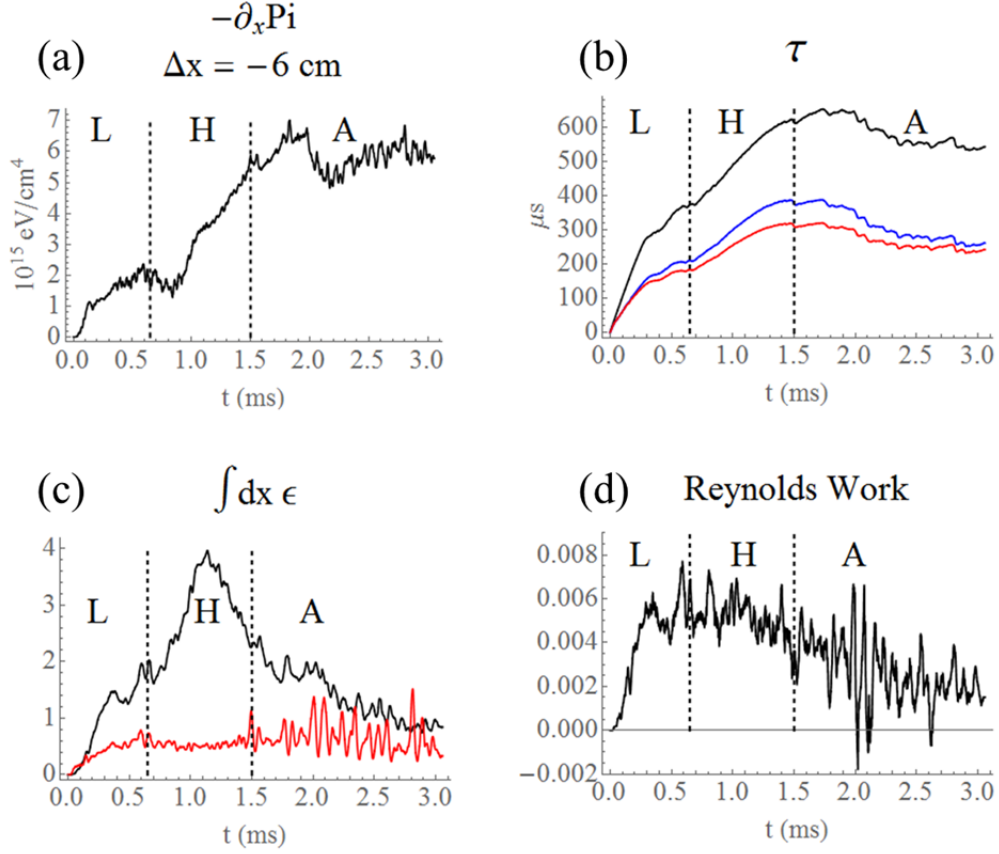


Fig. 2. Evolution of the (a) ion pressure gradient 6 cm inside the separatrix, (b) particle and energy confinement times (τ_n , τ_{Pe} , τ_{Pi}), shown as (black, blue, red) lines respectively, (c) mean, Eq. (A9) (black), and fluctuating, Eq. (A15) (red), flow energies and (d) Reynolds work Eq. (A14) for the ramped-source simulation. L and H indicate the low- and high-confinement regimes, and A denotes the avalanche regime. In (b) the integrals defining the confinement times (Eqs. 1 and 2) are over $\Delta x < 0$ and include the sources but not the SOL. In (c) and (d), integrals involved in the calculations are from $\Delta x = -7.5$ cm to $\Delta x = 0$ and so exclude the source-driven region and the SOL.

At early times, before the front detaches from the core, the ion pressure gradient rises at the foot of the heated region ($\Delta x = -8$ cm, see Fig. 1) and confinement times tend to saturate at relatively low values, as seen in Fig. 2(b); this is the L-regime. With increased heating, the front detaches from the heater boundary and propagates radially outward toward the edge region, and confinement times increase markedly; this is the H regime. The increased plasma pressure and density in the wake of the propagating front is responsible for the rise in confinement times. Confinement times continue to rise as the front reaches a neighborhood of the separatrix, and the expanding plasma begins to experience the parallel transport of the SOL. This SOL-overlap begins at about 1.1 ms and is seen as an inflection point in the τ -histories in Fig. 2(b) and as a corresponding peak in the mean-flow energy history of Fig. 2(c).

The H-regime ends, and the A-regime begins, when the confinement times start to decrease at $t = 1.5$ ms. Throughout the H-regime, the fluctuation energy Eq. (A15) (the red curve in Fig. 2(c)) is relatively quiet and constant in comparison to the intermittent bursts that follow. The bursts correspond to the step-wise reductions in confinement times, evident in Fig. 2(b), and to poloidally localized bursts in the radial particle flux at the separatrix for which this regime is named.

We conjecture that the H-regime is terminated, and the A-regime begins, as the flow-shear associated with the propagating front (which, it may be argued, serves to control the interchange instability at the front) is displaced by the high flow-shear imposed by the sheath physics in the SOL as the front approaches the separatrix, and that, with this transition, the K-H instability emerges to drive the avalanches. The following analysis of the turbulent flow energetics appears to support this scenario.

The Reynolds work, defined in the appendix, Eq. (A14), is the rate at which velocity fluctuations increase energy in the mean fluid flow. Where the work is positive the fluctuations beat together to manufacture mean flow, and where it is negative that beating depletes the mean flow (e.g. K-H instability). The Reynolds work history for the ramped-heater simulation is shown in Fig. 2(d). In the L- and H-regimes, the Reynolds work is positive, indicating a transfer of energy from the fluctuations to the mean flow. But in the A-regime, the mean Reynolds work decreases toward zero, with negative bursts in the instantaneous value clearly associated with the avalanches. Thus confinement deteriorates as energy is increasingly transferred from the mean flow to the fluctuations, supporting the speculation that the Kelvin-Helmholtz instability is responsible for terminating the H-mode. This energy analysis is global, i.e., the integrals in Eqs. 1 and 2, extend from $\Delta x = -7.5$ cm to the separatrix. Similarly, support for the first part of the conjecture, concerning shear-control of the interchange instability at the propagating front, may be gleaned by analyzing the Reynolds work at the front.

A standard model holds that the L-H transition may be triggered by a surge in Reynolds work that drives sheared mean flows that moderate the interchange instability and allow pressure gradients to rise. Signatures of this well-developed paradigm have been observed in many, though not all, experiments and simulations. (See the discussion and references in Sec. I.) Curiously, a similar sequence of events is observed as the front passes by a fixed reference point in this simulation. Histories of the normalized mean flow production rate [P_{mf} from Eq. (A12), divided by the turbulence production rate $\gamma_{mhd} \epsilon_{fl}$], the mean flow shear rate and the ion pressure gradient are plotted at a fixed radial location in Fig. 3. It is seen that as the mean flow production rate rises to equal the turbulence production rate, Fig. 3(a), the magnitude of the $E \times B$ flow shear rate, Fig. 3(b), rises to surpass the local interchange instability growth rate γ_{mhd} , and a rise in the ion pressure gradient, Fig. 3(c), follows. So locally it would appear that a surge in

Reynolds-driven sheared flow, acting to suppress the interchange instability, is followed by a rise in the ion pressure gradient, viz., a paradigmatic L-H transition has occurred. Note that the ratio $P_{mf}/(\gamma_{mhd} \epsilon_{fl})$ is order unity at the front, indicating efficient conversion of fluctuation energy to mean flow energy but not necessarily local moderation of the interchange instability by the sheared mean flow; the proof of this moderation is provided in Fig. 3(b).

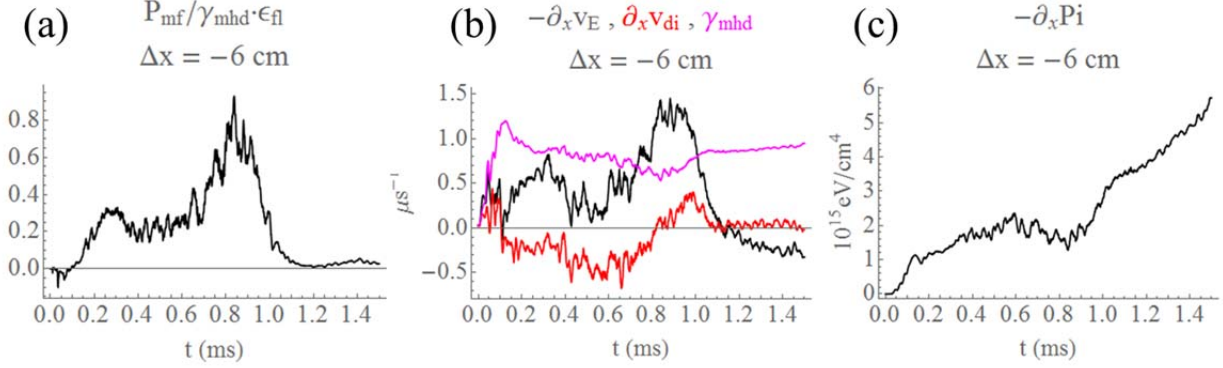


Fig. 3. Time evolution of (a) the mean flow production rate divided by the turbulence production rate (see the Appendix), (b) the $(-)\mathbf{E} \times \mathbf{B}$ flow shear rate (black) together with the shear rate of the ion diamagnetic drift (red) and the local interchange instability growth rate (magenta) and (c) the pressure gradient, all at a fixed radial location 6 cm inside the separatrix, spanning the L-H transition. Positive P_{mf} corresponds to the transfer of turbulent energy into mean-flow energy. Note that the ion pressure gradient begins to rise after the enhanced $\mathbf{E} \times \mathbf{B}$ flow shear rate has surpassed γ_{mhd} , at about $t = 0.8$ ms.

The shear rate of the ion diamagnetic drift is plotted in Fig. 3(b) along with that of the $\mathbf{E} \times \mathbf{B}$ drift. Although a weak effect, some “mirroring” of the two flows, i.e., $\partial_x v_E + \partial_x v_{di} \cong \text{constant}$, can be observed as the front approaches. Persistent mirroring would provide a route to an enduring H-mode in the wake of an L-H transition: with rising ion pressure gradient, the increasing $\mathbf{E} \times \mathbf{B}$ flow shear might continue to suppress the interchange instability and “lock-in” the H-mode. However, as we suspect is the case here, increasing shear rates may also drive the K-H instability and ruin the H-mode.

All regimes are transient in the ramped-source simulation. The L-regime lasts only until the front arrives, leaving the H-regime in its wake, and the H-regime subsides as avalanches set in. Nor has the A-regime reached equilibrium at the end of the simulation. We conducted a series of simulations with stationary sources, differing only in the amplitude of the ion heating

source, and discovered equilibria corresponding to the regimes visited in the ramped case. The confinement times for these simulations are plotted in Fig. 4.

In these stationary- S_{P_i} simulations, the L-regime is characterized by confinement times that *decrease* with increasing heater power, while the H-mode confinement times increase with increasing heater power. This loss of confinement with increasing heater power in the L-regime was not observed in the ramped case because the L-regime did not equilibrate before the front detached and propagated from the heater region. Otherwise the stationary simulations recover the confinement characteristics of the three regimes found in the ramped case, and the flow shear rate exceeds the interchange growth rate ($|\partial_x v_E| > \gamma_{\text{mhd}}$) within the turbulence birth zone in the H-regime, as it does at the propagating front in the ramped- S_{P_i} simulation.

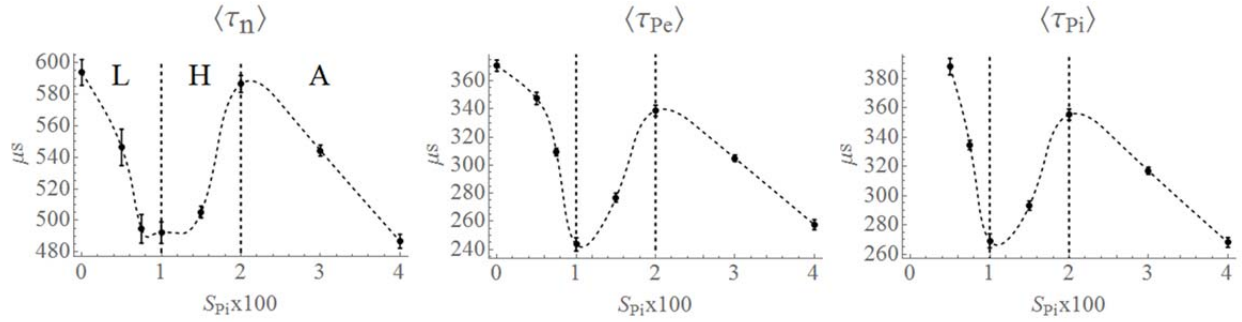


Fig. 4. Confinement times from seven simulations that used the same parameters as the ramped case except here the ion pressure source (S_{P_i}) was held fixed. Simulations were run to equilibrium in each case, and the confinement times were averaged over the last 0.5 ms, with error bars representing standard deviations about the averages.

IV. Role of the SOL in core confinement

In this section we study how the edge ($\Delta x < 0$) confinement times depend upon SOL ($\Delta x > 0$) collisionality. We ran a single simulation, with the parameters of Sec. V (Here we used fixed sources: $S_n = S_{P_i} = S_{P_e} = 0.01$.), but changed the SOL collisionality abruptly midway through the simulation. The resulting change in core confinement is shown in Fig. 5.

In the SOLT model, the SOL collisionality is described by a single parameter, $\Lambda = v_{ei} L_{||} / \Omega_e \rho_s = (m_e / m_i)^{1/2} L_{||} / \lambda_{ei}$: the ratio of volume plasma resistance to the effective sheath resistance. ($\Lambda \sim 0.01$ for the reference parameters used in the simulations in Sec. III, implying a sheath-connected regime.) Parallel transport in the SOL adjusts *self-consistently* between conduction-limited (CL) and sheath-limited (SL) expressions for the particle (charge) and heat fluxes, with CL electron parallel fluxes inversely proportional to Λ : $j_{CL}, q_{CL} \sim 1/\Lambda$. (See Appendix A of Ref. 18 for details.) The smaller of the CL and SL expressions dominate the total

flux via the (*time-dependent*) relation $1/j = 1/j_{\text{CL}} + 1/j_{\text{SL}} + 1/j_{\text{FL}}$ and similarly for the inverse heat flux $1/q$. (j_{FL} is an overall flux limit $\sim v_e$). At high collisionality, CL fluxes dominate parallel transport in the SOL, tending to disconnect the midplane from the divertor sheath.

At $t \cong 2$ ms (dashed vertical line in Fig. 5), Λ was changed from 10^8 (effectively “ ∞ ” for complete disconnection) to 10^{-5} (effectively “0” for connection) in the simulation. As shown in Fig. 5, at low-collisionality, sheath-limited transport results in larger confinement times than high-collisionality, disconnected transport. Furthermore it was verified (not shown explicitly here) that the transition is reversible.

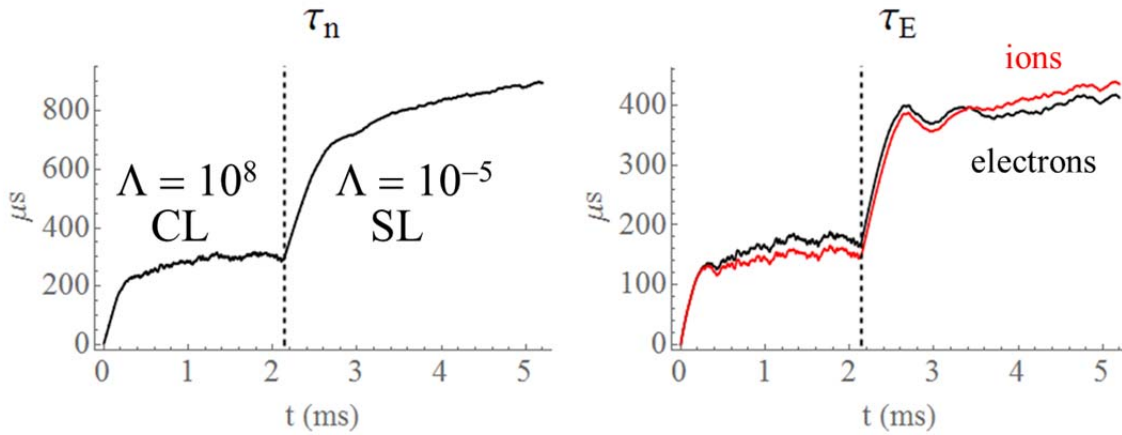


Fig. 5. History of edge particle and energy confinement times in a simulation with stationary sources. The SOL collisionality parameter was Λ decreased abruptly (manually) at $t \cong 2$ ms (dashed line), establishing sheath-connection and leading to improved confinement.

The characteristics of the CL-to-SL transition include: increased confinement times (Fig. 5); decreased normalized density fluctuation amplitudes (Fig. 6); decreased electrostatic potential fluctuation amplitudes (not shown); decreased SOL heat flux width (not shown); and a quiet interlude lasting about 200 μs immediately following sheath connection (not shown). Regarding the last point, a similar interlude was sometimes observed in NSTX experiments following the L-H transition.²⁴

It was found that sheath-connection brings significant change in the configuration of the sheared $E \times B$ flow. In the connected (SL) state a flow-shear layer controls the interchange instability in a neighborhood of the separatrix. See Fig. 7. The flow is dominated by sheath physics in the near-SOL; the sheath is controlling the perpendicular transport. This strong shear layer is absent in the disconnected (CL) regime. The profound effect of this change on the structure of the turbulence in the shear layer is illustrated in Fig. 8 which shows snapshots of the turbulent electron temperature and potential profiles in the CL and SL states. It is seen that

relatively large-scale separatrix-spanning vorticity cells dominate the turbulence in the low-confinement CL state. These structures are precluded by the flow-shear layer imposed by the sheath, Fig. 7(b), in the high-confinement SL state.

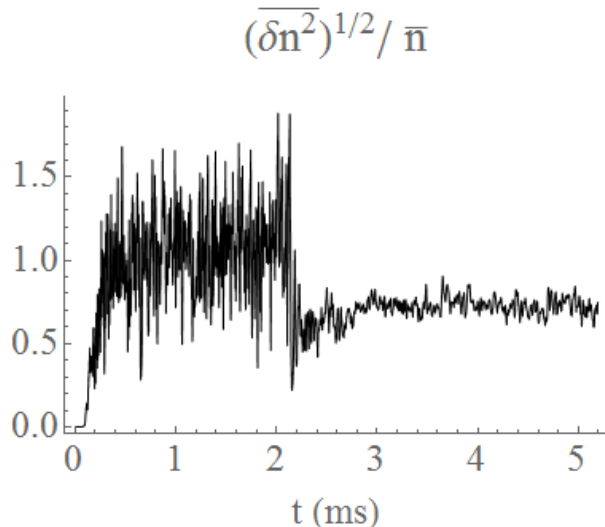


Fig. 6. History of normalized density fluctuations, at the separatrix, across the L-H transition that was induced by changes in SOL collisionality.

V. Summary and conclusions

In this report, we have investigated confinement regimes and confinement transitions using a two-dimensional, electrostatic, source-driven, fluid turbulence model that retains the ion diamagnetic and gyro-viscous effects. We find three different confinement regimes with increasing ion heating. The regimes L, H and A are reminiscent of tokamak L, H, and ELMy-H mode regimes. Our model does not have enough physics to describe the peeling-ballooning modes²⁵ that are believed to be essential in the tokamak ELMy-H mode regime; rather, our regime A likely involves the Kelvin-Helmholtz instability. Like the tokamak regimes, confinement first degrades with increasing heating power in L mode, improves with sufficient power to induce the L-H transition, and then degrades once again in the A regime where violent ejection events occur.

These three regimes were found in both ramped ion heat source simulations and in steady state simulations. In the ramped heating case, enhanced confinement in the H-regime is associated with the outward propagation of a shear layer to just inside the separatrix. Inside the shear layer, the radial gradient of the $E \times B$ velocity is seen to exceed the nominal interchange growth rate, $|v'_E| > \gamma_{mhd}$. We note that the relationships between v'_E , v'_{di} and pressure gradient

$\langle \gamma_{\text{mhd}} \rangle$ depend strongly on radial location, making local diagnosis ambiguous. To understand the dynamics of the transition a global energetics model, taking into account both $E \times B$ and diamagnetic velocities for both fluctuation and zonal flow energy, was developed and applied to the simulations. Results are broadly consistent with the driving of $E \times B$ flows by both the transfer of fluctuation energy and by the ion pressure gradient. Shear in the radial electric field appears to play an important role in enhancing confinement in the H-regime, but may also ultimately be responsible for confinement degradation in the A-regime.

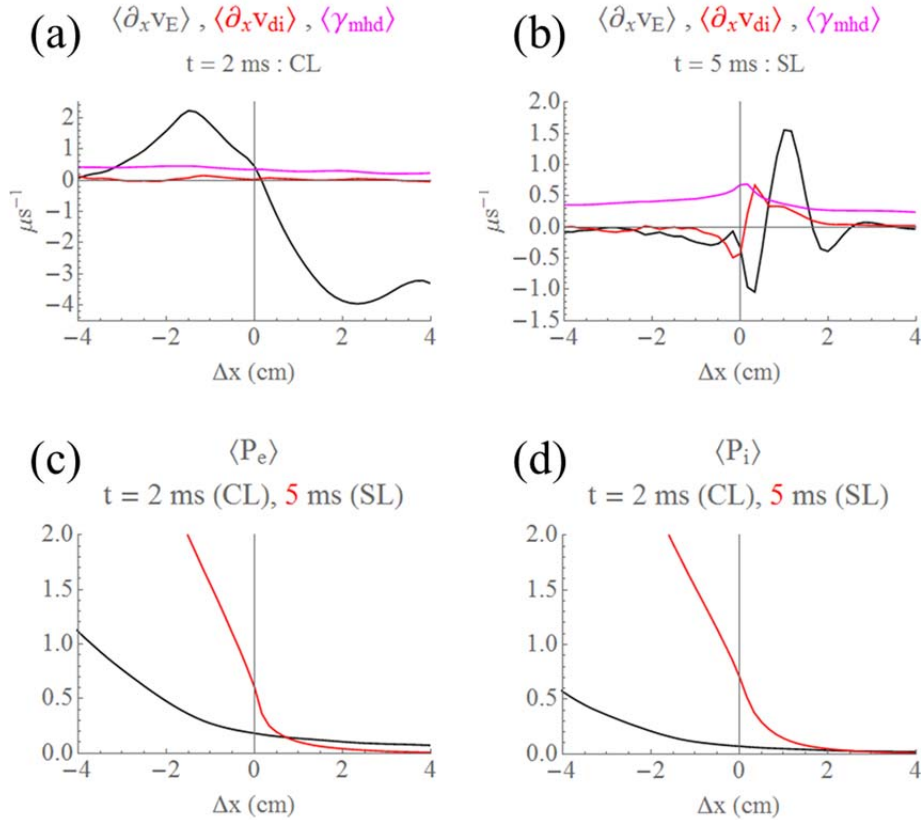


Fig. 7. Upper panels show the radial structure of the $E \times B$ flow shear, $\partial_x v_E$, ion diamagnetic shear, $\partial_x v_{\text{di}}$ and interchange growth rate γ_{mhd} : (a) for the disconnected (CL, L-mode) state, and (b) for the connected (SL, H-mode) state. Lower panels show the radial pressure profiles in the two confinement states: (c) electron pressure in the CL (black) and SL (red) states and (d) ion pressure in the CL (black) and SL (red) states. Angular brackets denote a time average over $100 \mu\text{s}$. The pressure is in Bohm units in (c) and (d).

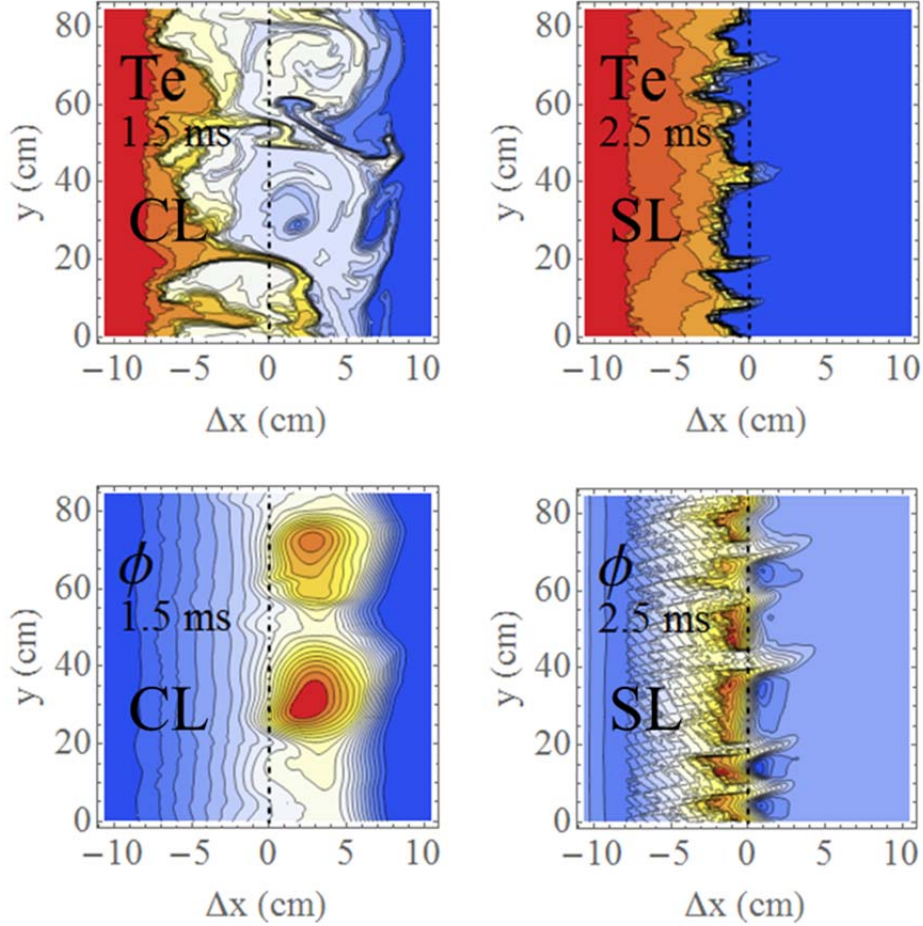


Fig. 8. Snapshots of the turbulent electron temperature and electrostatic potential in the CL (left column) and SL (right column) states.

Finally an important role for SOL collisionality on the confinement time has been demonstrated. The ratio of volume plasma resistance to the effective sheath resistance, described by the parameter Λ , is the control parameter. Sheath-limited parallel transport in the SOL ($\Lambda < 1$) is characterized by higher edge particle and energy confinement times than collision-limited parallel transport ($\Lambda > 1$). Disconnecting the sheath by increasing the SOL collisionality parameter Λ results in an H-L back-transition; reconnecting the sheath by decreasing the parameter Λ results in an L-H transition.

Clearly the reduced model employed in these studies omits many details which are likely to affect confinement transitions in tokamak experiments (e.g. three-dimensional geometry, neutral-plasma interactions, kinetic effects, electromagnetic effects). Nevertheless, the present

results emphasize the importance of moving transition fronts, ion fluctuation energy and total energy dynamics, Kelvin-Helmholtz instabilities, and SOL collisionality on the fundamentals of L-H transition dynamics.

Acknowledgements

This material is based upon work supported by the U.S. Department of Energy Office of Science, Office of Fusion Energy Sciences under Award Number DE-FG02-97ER54392.

Appendix A: Turbulent flow energetics with finite ion pressure

In this appendix, we generalize the usual cold fluid Boussinesq description of turbulent energetics to the finite ion pressure non-Boussinesq model. The Boussinesq and cold ion limits are easily obtained as special cases of the present calculation. (See. e.g. Ref. 4 for a concise summary of the cold ion limit.) Bohm units are employed throughout (i.e. with time and space normalizations $1/\Omega_i$ and ρ_i respectively) and the magnetic field is taken to be constant in space.

Let the total mass flow velocity be

$$\mathbf{u} = \mathbf{v}_E + \mathbf{v}_{di} \quad (\text{A1})$$

where $\mathbf{v} \equiv \mathbf{v}_E = \mathbf{b} \times \nabla \Phi$ and $n\mathbf{v}_{di} = \mathbf{b} \times \nabla p_i$. For notational simplicity in the following, we drop the subscript E on \mathbf{v}_E . It follows that $\langle v_x \rangle = 0$ where here and in the following $\langle \dots \rangle$ is a y-average. The momentum-density per unit mass and particle flux are given by

$$\mathbf{g} = n\mathbf{u}. \quad (\text{A2})$$

Considering a uniform B-field, with density source S_n , the basic conservation equations for n and \mathbf{g} are

$$\partial_t n + \nabla \cdot (n\mathbf{v}) = S_n \quad (\text{A3})$$

$$\partial_t \mathbf{g} + \nabla \cdot (n\mathbf{g}) = 0. \quad (\text{A4})$$

For future reference, we can also write an equation for the velocity \mathbf{u} as

$$\partial_t \mathbf{u} + \mathbf{v} \cdot \nabla \mathbf{u} = -\mathbf{u} S_n / n. \quad (\text{A5})$$

By taking $\mathbf{b} \cdot \nabla \times$ of Eq. (A4), it can be shown [see e.g. the Appendix of Myra 2016] that the inertial terms represented by the left-hand-side of Eq. (A4) are equivalent to the evolution of generalized vorticity given by

$$\partial_t \varpi + \mathbf{v} \cdot \nabla \varpi + \frac{1}{2} \nabla \cdot [\nabla(\mathbf{v} \cdot \nabla p_i) - \varpi \mathbf{v} + (n \nabla^2 \Phi)(\mathbf{v} + \mathbf{v}_{di}) + (\mathbf{v} \cdot \nabla n)(\nabla \Phi)] = 0 \quad (\text{A6})$$

where $\varpi = \nabla \cdot (n \nabla \Phi + \nabla p_i)$. Eq. (A6), supplemented with parallel current and curvature terms, is just the SOLT equation for vorticity evolution, hence, in considering a turbulent flow energetics model with finite ion pressure, it is sufficient to work with the algebraically simpler form of Eqs. (A4) or (A5).

The energy density per unit mass is $\mathbf{g} \cdot \mathbf{u} / 2$ and an energy evolution equation is obtained from $\mathbf{u} \cdot \text{Eq. (A4)} + \mathbf{g} \cdot \text{Eq. (A5)}$. After a simple manipulation we find

$$\frac{1}{2} \partial_t (\mathbf{u} \cdot \mathbf{g}) + \frac{1}{2} \nabla \cdot (\mathbf{v} \mathbf{u} \cdot \mathbf{g}) = -\frac{S_n}{2n} \mathbf{u} \cdot \mathbf{g}. \quad (\text{A7})$$

Taking a y -average of this energy equation yields

$$\partial_t \varepsilon + \partial_x q = -S_\varepsilon \quad (\text{A8})$$

with $\varepsilon = \langle \mathbf{u} \cdot \mathbf{g} \rangle / 2$, $q = \langle v_x \mathbf{u} \cdot \mathbf{g} \rangle / 2$, $S_\varepsilon = \langle S_n u^2 \rangle / 2$. The term on the right-hand-side of Eq. (A8) is negative, reflecting the fact that particles sources added at zero momentum require an energy cost to bring them up to the local velocity of the fluid.

There can be some latitude in how we split the energy into zonal (“mean”) flow and fluctuating contributions. It is easiest to *define* the zonally-averaged flow energy as

$$\varepsilon_{mf} = \frac{1}{2} \langle \mathbf{u} \rangle \cdot \langle \mathbf{g} \rangle \quad (\text{A9})$$

To obtain an equation for the zonal flow, first take the y -average of Eqs. (A4) and (A5) and then combine by dotting with $\langle \mathbf{u} \rangle$ and $\langle \mathbf{g} \rangle$ respectively and adding to obtain

$$\partial_t \varepsilon_{mf} + \partial_x q_{mf} = P_{mf} - S_{mf} \quad (\text{A10})$$

where the zonal flow energy flux is

$$q_{mf} = \frac{1}{2} [\langle \mathbf{g} \rangle \cdot \langle v_x \mathbf{u} \rangle + \langle \mathbf{u} \rangle \cdot \langle v_x \mathbf{g} \rangle], \quad (\text{A11})$$

the zonal flow production term is

$$P_{mf} = \frac{1}{2} [\langle v_x \mathbf{u} \rangle \cdot \partial_x \langle \mathbf{g} \rangle + \langle v_x \mathbf{g} \rangle \cdot \partial_x \langle \mathbf{u} \rangle], \quad (\text{A12})$$

and the energy loss term due to particle sources (at zero velocity) is

$$S_{mf} = \left\langle \frac{S_n}{2n} \mathbf{u} \right\rangle \cdot \langle \mathbf{g} \rangle. \quad (\text{A13})$$

$P_{mf} > 0$ implies energy transfer from fluctuations to mean flow and $P_{mf} < 0$ implies turbulence production from mean flows (e.g. KH instability).

The Reynolds work can be defined as the rate of change of volume-integrated mean-flow energy from Eq. (A10), i.e.

$$R_w \equiv \partial_t \int dx \varepsilon_{mf} = -\Delta q_{mf} + \int dx (P_{mf} - S_{mf}) \quad (\text{A14})$$

where Δq_{mf} is the difference in q_{mf} at the integration boundaries.

The fluctuation energy is then *defined* as the difference of the y-averaged total energy and the zonal flow energy

$$\varepsilon_{fl} = \varepsilon - \varepsilon_{mf} = \frac{1}{2} (\langle \mathbf{u} \cdot \mathbf{g} \rangle - \langle \mathbf{u} \rangle \cdot \langle \mathbf{g} \rangle) = \frac{1}{2} \langle \tilde{\mathbf{u}} \cdot \tilde{\mathbf{g}} \rangle, \quad (\text{A15})$$

where \mathbf{u} and \mathbf{g} are expanded, e.g. as $\mathbf{u} = \langle \mathbf{u} \rangle + \tilde{\mathbf{u}}$. Subtracting the total and zonally-averaged flow energy equations, and carrying out some simple manipulations

$$\partial_t \varepsilon_{fl} + \partial_x q_{fl} = -P_{mf} - S_{fl}, \quad (\text{A16})$$

where

$$q_{fl} = q - q_{mf} = \frac{1}{2} \langle v_x \tilde{\mathbf{u}} \cdot \tilde{\mathbf{g}} \rangle \quad (\text{A17})$$

and

$$S_{fl} = S_\varepsilon - S_{mf} = \left\langle \frac{S_n}{2n} \mathbf{u} \cdot \tilde{\mathbf{g}} \right\rangle. \quad (\text{A18})$$

In obtaining Eq. (A17) we have used $\langle v_x \rangle = 0$. The term $\partial_x q_{fl}$ is sometimes called the turbulence spreading term.

In the main text, the definitions of mean flow and fluctuating energies, their fluxes and the definition of zonal flow production are employed to analyze the simulations. In the

simulations, the evolution of these quantities is of course influenced not just by the conservative terms manipulated here, but also by instability growth, heat sources, flow damping and losses of particles energy and momentum to the sheaths.

In the limit of cold ions, and furthermore making the often-invoked Boussinesq approximation, the energies, fluxes and production term reduce to the familiar forms

$$\varepsilon_{mf} = \frac{n}{2} \langle v_y \rangle^2 \quad (\text{A19})$$

$$q_{mf} = \frac{n}{2} \langle v_x v_y^2 \rangle \quad (\text{A20})$$

$$P_{mf} = n[\langle v_x v_y \rangle \partial_x \langle v_y \rangle] \quad (\text{A21})$$

$$\varepsilon_{fl} = \frac{n}{2} \langle \tilde{v}^2 \rangle \quad (\text{A22})$$

$$q_{fl} = \frac{n}{2} \langle v_x \tilde{v}^2 \rangle \quad (\text{A23})$$

However, in the present simulations these Boussinesq forms for $T_i = 0$ are poor approximations to the full expressions.

References

- ¹ F. Wagner, G. Becker, K. Behringer, D. Campbell, A. Eberhagen, W. Engelhardt, G. Fussmann, O. Gehre, J. Gernhardt, G. v. Gierke, et al., Phys. Rev. Lett. **49**, 1408 (1982).
- ² G. R. Tynan, I. Cziegler, P. H. Diamond, M. Malkov, A. Hubbard, J. W. Hughes, J. L. Terry and J. H. Irby, Plasma Phys. Control. Fusion **58**, 044003 (2016).
- ³ M. A. Malkov et al. Phys. Plasmas **22**, 032506 (2015).
- ⁴ I. Cziegler et al., Plasma Phys. Control. Fusion **56**, 075013 (2014).
- ⁵ G.S. Xu et al., Nucl. Fusion **54**, 103002 (2014).
- ⁶ L. Schmitz et al., Nucl. Fusion **54**, 073012 (2014).
- ⁷ C. Bourdelle et al., Nucl. Fusion **54**, 022001 (2014).

- ⁸ A. Diallo, S. Banerjee, S. Zweben, and T. Stoltzfus-Dueck, “Energy Exchange Dynamics across L-H Transitions in NSTX,” 26th IAEA Fusion Energy Conference, Kyoto, Japan, 17-22 October 2016, IAEA-CN-234/EX/5-3.
- ⁹ L. Chôné et al., Nucl. Fusion **55**, 073010 (2015).
- ¹⁰ J. J. Rasmussen, A. H. Nielsen, J. Madsen, V. Naulin and G. S. Xu, Plasma Phys. Control. Fusion **58**, 014031 (2015).
- ¹¹ G.Y. Park et al., Phys. Plasmas **22**, 032505 (2015).
- ¹² L. Chôné et al., Phys. Plasmas **21**, 070702 (2014).
- ¹³ G.M. Staebler and R.J. Groebner, Nucl. Fusion **55**, 073008 (2015).
- ¹⁴ B. Li, X. Y. Wang, C. K. Sun, A. Zhou, D. Liu, C. H. Ma, and X. G. Wang, Phys. Rev. E **94**, 043201 (2016).
- ¹⁵ C. S. Chang, S. Ku, G. Tynan, R. Hager, R. Churchill, I. Cziegler, M.Greenwald, A. E. Hubbard and J. W. Hughes, “A fast L-H bifurcation dynamics in a tokamak edge plasma gyrokinetic simulation,” submitted to Phys. Rev. Lett. (2017).
- ¹⁶ L. Schmitz, Nucl. Fusion **57**, 025003 (2017).
- ¹⁷ D. A. Russell, J. R. Myra, and D. A. D’Ippolito, Phys. Plasmas **16**, 122304 (2009).
- ¹⁸ D. A. Russell, D. A. D’Ippolito, J. R. Myra, J. M. Canik, T. K. Gray, and S. J. Zweben, Phys. Plasmas **22**, 092311 (2015).
- ¹⁹ K. Miki, P. H. Diamond, S.-H. Hahn, W.W. Xiao, Ö. D. Gürçan, and G. R. Tynan, Phys. Rev. Lett. **110**, 195002 (2013).
- ²⁰ T. Estrada, E. Ascasíbar, E. Blanco, A. Cappa, F. Castejón, C. Hidalgo, B.Ph. van Milligen and E. Sánchez, Nucl. Fusion **55**, 063005 (2015).
- ²¹ T. Kobayashi, K. Itoh, T. Ido, K. Kamiya, S.-I. Itoh, Y. Miura, Y. Nagashima, A. Fujisawa, S. Inagaki, K. Ida, and K. Hoshino, Nucl. Fusion **55**, 063009 (2015) .
- ²² J.R. Angus and M.V. Umansky, Phys. Plasmas **21**, 012514 (2014).
- ²³ M. Wakatani and A. Hasegawa, Phys. Fluids **27**, 611 (1984).
- ²⁴ R.J. Maqueda, D.P. Stotler, S.J. Zweben, The NSTX team, J. Nucl. Mater. **415**, S459 (2011).
- ²⁵ P.B. Snyder, R.J. Groebner, J.W. Hughes, T.H. Osborne, M. Beurskens, A.W. Leonard, H.R. Wilson and X.Q. Xu, Nucl. Fusion **51**, 103016 (2011).